Organosilicon modified method to improve Li$^+$ storage capacity of graphene oxide (GO)

WANG Kun[2], JU DongYing[2,3], XU GuiYing[1*], HAN BeiBei[3], CHAI MaoRong[3], WANG YingXin[4], Li LiXiang[1], ZHANG XueHu[1], UCIDA Masaya[3] & ZHOU WeiMin[1*]

[1]*Key Laboratory of Energy Materials and Electrochemistry Research Liaoning Province, School of Chemical Engineering, University of Science and Technology Liaoning, Anshan 114051, China;*
[2]*School of Materials and Metallurgy, University of Science and Technology Liaoning, Anshan 114051, China;*
[3]*Advanced Science Research Laboratory, Saitama Institute of Technology, 1690 Fusaiji, Fukaya, Japan;*
[4]*JiXi Weida New Material Technology Co., Ltd, Jixi 158100, China*

Organosilicon modified reduced graphene oxide (MrGO) has been fabricated by direct organosilicon modification of graphene oxide (GO). Interestingly, it is observed that 3D rGO-like structures occurred after directly carrying out the organosilicon modification on the surface of GO. The obtained organosilicon MrGO displays the more remarkable improvement of electrochemical performances than GO, which was verified by electrochemical measurements in detail. For instance, the organosilicon MrGO shows the cycling performances at 901 mA h g^{-1} after 200 cycles at 0.1 A g^{-1} and 446 mA h g^{-1} after 300 cycles at 2.0 A g^{-1}, respectively. These results unveil that organic modification method is an effective way to improve the Li$^+$ storage capacity of general carbon materials.

graphene oxide (GO), surface modification, organosilicon modification, 3D rGO-like structure, organic-inorganic concept, lithium ion batteries (LIBs)

1   Introduction

Recently, the graphene as functional carbon material has been exponentially intrigued than ever before, for it has special structure and charming properties such as excellent mechanical strength, high chemical stability, superior conductivity, and thermal conductivity [1–4]. Therefore, the graphene has been known as next-generation materials in fabrications of Li$^+$ storage materials for lithium ion batteries (LIBs). However, some defects restrict the graphene in actual fabrications of LIBs as electrode materials. Thereinto, the latest researches expound that Li$^+$ ions show the instability and low diffusion ability in structures of graphene, decreasing the Li$^+$ storage capacity of graphene.

To expand the actual applicability of graphene as electrode materials, a lot of methods are unfolded and used to improve the Li$^+$ storage capacity of graphene. For instance, a number of researchers attempt to introduce the active sites in the graphene to boost the charge-discharge capacity of Li$^+$ ions. Nevertheless, the problem of overlapping among layers of graphene cannot be solved well [5]. As a consequence, other methods such as mixing the nano metallic oxide or making the graphene to have the 3D structure are used to overcome the overlapping problem among layers of graphene [6–9]. Especially, fabrication of 3D graphene having the porous

---

*Corresponding authors (email: xuguiying751107@163.com; aszhou15242870697@163.com)

structures is becoming a hot research topic gradually, for possessing the relatively low cost and porous structures of 3D graphene is able to improve the Li^+ transfer effectively [10–13].

On the other hand, in our previous studies, based on the inorganic-organic hybrid concept, we embark on introducing the organosilicon groups on the surface of carbon black (CB) via the modified reactions of CB with tert-butyldimethylsilyl chloride [14]. As a result, after introducing the organosilicon groups on the surface of CB, the electrochemical performances of modified CB (MCB) were improved remarkably, which reveals the organic modification way is an effective method improving the Li^+ storage capacity of general carbon materials.

In these presented studies, we attempt to use the same method as organosilicon modification to improve the Li^+ storage capacity of GO. Interestingly, the 3D reduced GO (rGO)-like structures appeared after the direct organosilicon modification of GO, which is verified by measurements of scanning electron microscope (SEM), transmission electron microscope (TEM), X-ray diffraction (XRD) and Brunauer-Emmett-Teller (BET). The organosilicon MrGO shows the remarkable improvement of Li^+ storage performances, which is verified by electrochemical studies in detail. For example, the organosilicon MrGO shows the cycling performances at 901 mA h g^{-1}, after carrying out the Li^+ charge-discharge 200 times. Meanwhile, organosilicon MrGO also exhibits the stability for the high current, which shows cycling performance at 446 mA h g^{-1}, after cycling 300 times at 2.0 A g^{-1}. In the Li^+ storage mechanism, we infer that formation of 3D structure and increased specific surface area of organosilicon MrGO lead to the amount of Li^+ intercalation became higher than the GO. In addition, the introducing of organosilicon groups can increase the capacitive effect, for the oxygen element on the $-COSiR_3$ and $-COOSiR_3$ groups can provide the surface reaction sites and defects for Li^+ storage [15].

2   Experiments

2.1   Materials

Trimethylsilyl chloride (TMCS, purity ≥ 98.5%) was purchased from SIYU chemical technology industrial (China) Ltd. Tetrahydrofuran (THF, purity ≥ 99.0%), triethylamine (purity ≥ 99.0%), natural graphite (325 mesh, purity > 99.85%), and phosphorus pentoxide (purity ≥ 98.0%) were purchased from Sinopharm Chemical Reagent, Co., Ltd, China. Potassium permanganate (purity ≥ 99.5%) and 30% hydrogen peroxide were purchased from Beijing organic chemical plant, China. The electrolyte of 1 mol L^{-1} $LiPF_6$ was obtained by dissolving the $LiPF_6$ in the mixture constructed by the ethylene carbonate/ethyl methyl carbonate/dimethyl carbonate (1:1:1, vol%). The electrolyte was pur-

chased from Bejing Institute of Chemical Reagents.

2.2   Characterization

The FT-IR results were determined by the instrument of Nicolet Company, USA. The measurements of XRD were carried out by X'pert Powder instrument with Cu-Kα radiation source (λ=1.5418 Å) from PANalytical, Holland. SEM morphologies were evaluated by ZEISS IGMA/HD instrument of Carl Zeiss AG, Germany. TEM measurement was carried out by the HF-3300 Hitachi, Ltd., Japan. The X-ray photoelectron spectroscopy (XPS) measurement was carried out by Quantum 2000 instrument of Physical Electronics, USA. Nitrogen adsorption and desorption isotherms were measured by QuadrasorbSI-MP which was purchased from Quantachrome Instruments, USA. Specific surface areas were determined by the BET method. The pore size distribution was calculated by the density functional theory (DFT) method. Electrochemical measurements were performed by the electrochemical system (CHI660E) of Chen-Hua, Shanghai, China. Table type high speed centrifuge was purchased from Shanghai Fichal Analytical Instrument Co., Ltd., China.

2.3   Silicone-modified reactions

Then GO (100 mg) was added into the THF solvent (30 mL), and dispersed by ultrasonic shaking process for 1 h, the TMCS (0.34 mL) and triethylamine (0.37 mL) were added and organosilicon modification was carried out for 24 h. Similarly, the analogous modification was carried out using the TMCS (0.61 mL) and triethylamine (0.67 mL). After filtering, the obtained solids were placed in vacuum drying oven to remove THF solution at room temperature. Finally, the obtained solids were carried out sublimation process to directly remove the triethylamine hydrochloride at 120°C for 12 h in a vacuum oven.

2.4   Electrochemical measurements

The electrochemical cells were prepared using the GO and organosilicon MrGO. Firstly, GO (0.08 g) or organosilicon MrGO (0.08 g) were respectively mixed with acetylene black (0.01 g) and polyvinylidine fluoride (PVDF) binder (0.01 g) in a weight ratio of 80:10:10 in *N*-methyl-2-pyrrolidone (NMP) solution. The obtained slurry was coated on the Cu foil and dried in vacuum drying oven at 80°C for 1 h to remove solution. Subsequently, the Cu foil with the active materials were dried at 120°C for 12 h in the same vacuum drying oven and cut into round shape strips of φ 11 mm in size. The mass loading of the active materials was controlled at 0.70 mg cm^{-2}. The two-electrode electrochemical cells (CR2032 coin-type) were assembled in a glove box filled

with high-purity argon, in which cells were assembled using the lithium metal foil (φ 15.60 mm × 0.45 mm) as reference electrode, Celgard 2400 microporous membrane as separator, and 12–13 wt% of $LiPF_6$ in the mixture of EC, DMC, EMC as electrolyte. Galvanostatic charge-discharge test was carried out by LAND (CT 2001A) battery test system in the voltage range of 0.05–3.0 V. The same electrochemical cells were also used to carry out measurements of CV. Cyclic voltammetry (CV) and electrochemical impedance spectroscopy (EIS) measurements were carried out by the CHI 660E. The cyclic voltammetry curves were recorded in the voltage region of 0.05–3.0 V at different scan rates. The impedance spectra were recorded in a frequency range of 100 kHz–0.01 Hz.

3   Results and discussion

First of all, the GO was fabricated by hummer method and dried at 120°C for 12 h before organosilicon modification [16]. The total mole number of –COOH and –OH on the surface of GO was investigated by the Boehm method [17]. Considering the complexity of modified reactions on the surface of GO, we intentionally used the excess TMCS to perform the organosilicon modifications. As an example, the TMCS was used as 5 and 9 times against the total mole number of –COOH and –OH on surface of GO to carry out modifications. In order to describe easily as following, the organosilicon modified materials were named as 5Si-rGO

and 9Si-rGO respectively. After carrying out the organosilicon modification, the yellow colour of GO was changed to the gray (Figure S1). It is different from the general purification methods using the solvent to wash the organosilicon MrGO. We adopt the sublimation method to directly evaporate the residual product of triethylamine hydrochloride. After the sublimation, the gray colour of solid changed to the black colour. In addition, after collecting, the structure of evaporated white solid was triethylamine hydrochloride, which was verified by FT-IR measurements (Figure S2).

On the other hand, the structures of organosilicon groups on the surface of GO and 9Si-rGO were verified by FT-IR measurements (Figure S3). Compared to the Figure S3(a), the new peak of 2920 cm^{-1} attributing to the alkyl groups on the Si element was observed clearly, which revealed that the $–COSiR_3$ and $–COOSiR_3$ groups were introduced on the surface of GO successfully (Figure S3(b)). Meanwhile, the characteristic peak belonging to the -C-O-Si group was also observed at 1165–1212 cm^{-1}, which also indicated the organosilicon modification performed successfully (Figure S3 (b)).

The XPS measurements were also used to validate the surface conversions of organosilicon modified GO from another perspective (Figure 1(a)–(c)). Compared to the GO, the novel peaks of ~101.3 eV (Si 2p) and ~152.7 eV (Si 2s) attributing to the organosilicon groups were observed markedly, which also was indicative of that organosilicon modification was carried out successfully [18]. In addition, the -C-C, -C-O, -C=O, -COO groups on GO surface showed
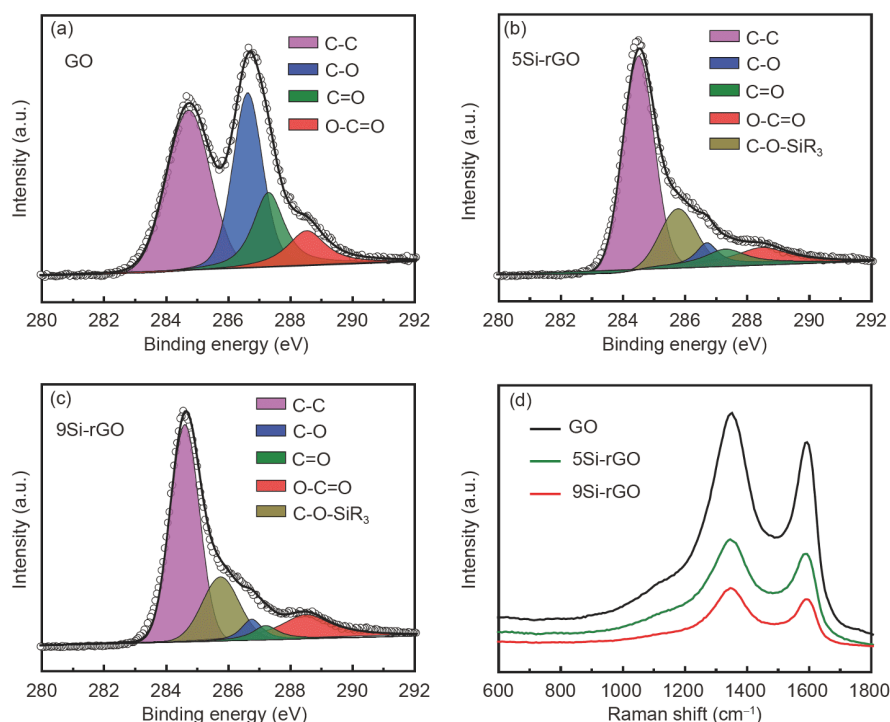

Figure 1   (Color online) XPS results (a)–(c) and Raman spectra (d) of samples.

the binding energy peaks at 284.7, 286.6, 287.3 and 288.6 eV, respectively, which was observed clearly. Meanwhile, with the decreasing of these peaks, the new peak at 285.7 eV attributing to the peaks of -C-OSiR groups appeared noticeably (Figure 1(b) and (c)) [19]. The XPS results also provided the strong evidence for that organosilicon groups were successfully introduced on the surface of organosilicon MrGO.

Based on aforementioned FT-IR and XPS analyses, the –OH and –COOH groups existing on the surface of GO were modified to the –COSiR$_3$ and –COOSiR$_3$ groups (Scheme S1). It is undeniable that epoxy groups existing on the surface of GO are also able to react with TMCS when the excess triethylamine existed, therefore, the epoxy groups could be reduced to the –COSiR$_3$ groups. As a result, the –COSiR$_3$ groups were also produced. At present stage, we take the attitude that Scheme S1 is rational to some extent.

The structures of GO and organosilicon MrGO were verified by XRD measurements. As shown in Figure 2, the characteristic peak at 11° attributing to the GO was expressly observed, indicating the GO was prepared successfully [20]. Interestingly, in the organosilicon MrGO, the new broad peak attributing to the (002) at around 23° was observed in 5Si-rGO, indicating the part of GO was reduced to the rGO after organosilicon modification [21–24].

Furthermore, to increase the ratio of rGO structure, the modified amount of TMCS was increased, and the 9Si-rGO was obtained. As a result, the characteristic peak at 11° disappeared completely and broad peak was observed clearly (Figure 2). The (002) peak can be fitted into one fitting peak at 2θ=23°, which indicated the 9Si-rGO possesses the rGO-like structure (Figure S4). Compared with the general rGO
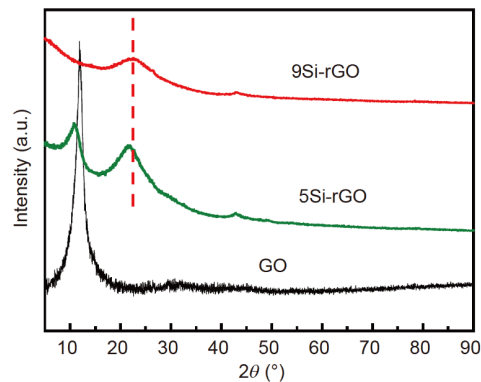

Figure 2   (Color online) XRD results of GO and organosilicon MrGO.

[25], the broad 002 peak of 9Si-rGO reveals that the graphitic layer of 9Si-rGO is not aligned. It was naturally attributed to the influence of introduced organosilicon groups on the surface of 9Si-rGO.

Compared to the GO, the distinct change of structure of GO was not observed (Figure 3(a)), after the heating process at 120°C for 12 h (Figure S5). In contrast, the porous structures clearly appeared in the 5Si-rGO and 9Si-rGO (Figure 3(b) and (c)). In accordance with the reports of Liu et al. [26,27], and based on the SEM and TEM measurement results, it is indicative of that 9Si-rGO simultaneously possessed the graphene sheets and macroporous structures (Figures 3(c) and S6). Morphology images of 9Si-rGO (Figure S6(b)) manifest the disordered graphene layers, which corresponds to the results of XRD, implying the existence of defects and organosilicon groups exist on the graphene sheets. It is worth mentioning that such structural damages are beneficial for electrochemical reactions [10].
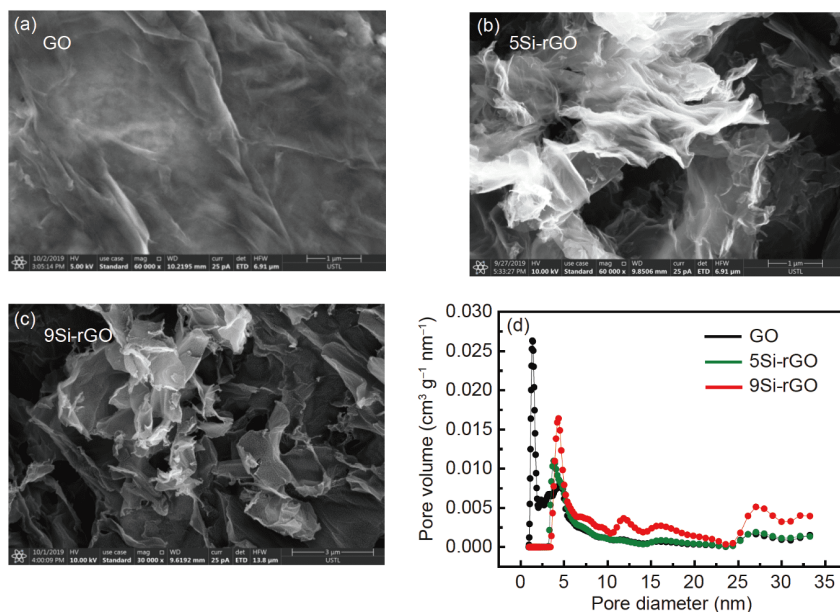

Figure 3   (Color online) SEM morphologies (a)–(c) and pore size distribution curves (d).

To investigate the conversions of structures of organosilicon MrGO before and after organosilicon modification, the nitrogen adsorption and desorption measurements were carried out in detail. As shown in Figure 3(d), in the range of 10–33 nm, the porous structures of 9Si-rGO became more complex than the GO and 5Si-rGO obviously. Meanwhile, a lot of pores having the pore size around 4.4 nm appeared in 9Si-rGO. Concurrently, as shown in Table S1, the surface area (m^2/g) and total pore volume (cm^3/g) of organosilicon MrGO were smaller than GO, for the heating treatment at 120°C decreased the surface area and pore volume. However, the surface area and total pore volume increased with increasing the modification amounts of TMCS (Table S1). These results revealed that structure of 9Si-rGO became more complex than GO and 5Si-rGO, with increasing the quantity of introduced organosilicon groups on the surface of modified GO. It leads us to consider that organosilicon modification occurred on the surface of GO plays the main role to change the characteristic structures from GO to organosilicon MrGO.

The differences of structures of GO, 5Si-rGO and 9Si-rGO were also investigated by the Raman measurements (Figure 1(d)). The characteristic peaks of D and G of graphite were observed at 1355 and 1600 cm^{-1} respectively [28]. Moreover, it is acknowledged that I_D/I_G values reflected the disordering of general carbon materials. In addition, to obtain the accurate I_D/I_G values, the D peak was fitted to the 3 peaks by origin software [29–32]. The fitting results of I_D and I_G from the Raman spectra were shown in Figure S7. As a result, the I_D/I_G values GO, 5Si-rGO, 9Si-rGO showed at 1.45, 1.68 and 1.74, respectively, indicating the 9Si-rGO possessed the more unordered structure than GO and 5Si-rGO. Compared to the GO, although the I_D/I_G value of GO decreased obviously (after carrying out the heating process at 120°C for 12 h), the increasing of I_D/I_G values of organosilicon MrGO reflected the distinct effect of introducing the organosilicon groups on the surface of organosilicon MrGO (Table S2).

In order to investigate the conversions of surface of organosilicon MrGO, the hydrophobicity was evaluated by the measurements of contact angle. As shown in Figure 4, the hydrophobicity of surface of 9Si-rGO became really stronger than GO and 5Si-rGO, which effectively revealed that organosilicon modification of 9Si-rGO performed completely. Similar to the report [33], the hydrophobicity improved by introducing the organosilicon groups is also able to facilitate the infiltration of electrolyte into interface of 9Si-rGO.

As shown in Figure 5(a), the rate performances were evaluated by continuously carrying out the charge-discharge cycles 10 times at different current density such as 0.1, 0.2, 0.5, 1.0 and 2.0 A g^{-1}. After the above evaluated measurements had been performed, the 9Si-rGO still showed the Li$^+$ storage capacity at 896 mA h g^{-1} when the current density
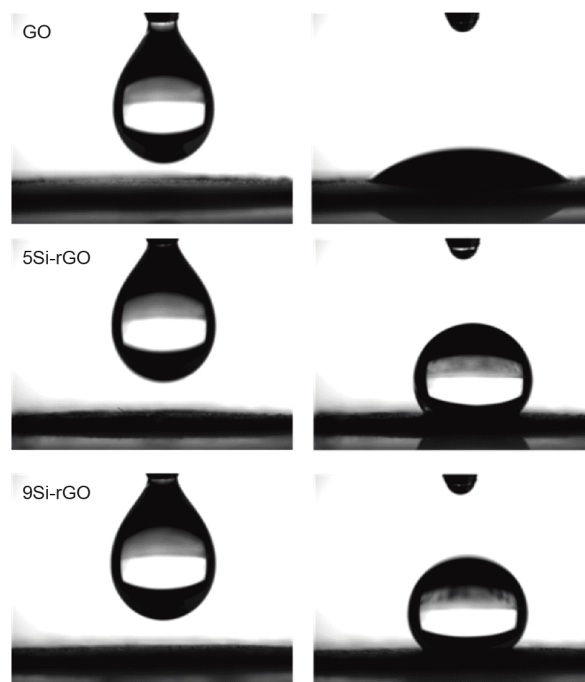

Figure 4 Contact angle results of GO and organosilicon MrGO.

was adjusted to the 0.1 A g^{-1} again, which was higher than the GO (223 mA h g^{-1}) and 5Si-rGO (296 mA h g^{-1}). These results revealed that 9Si-rGO possessed remarkable improvement of rate performances, compared with the GO and 5Si-rGO.

Similar to the general carbon materials, the obvious charge-discharge plateau was not observed in charge-discharge curves of GO, 5Si-rGO and 9Si-rGO (Figure 5(b) and S8). According to the charge-discharge measurements, the 9Si-rGO showed first Coulomb efficiency at 62.2%, which was higher than the GO (37.6%) and 5Si-rGO (50.3%), respectively. The high first coulomb efficiency of 9Si-rGO was attributed to the –OH and –COOH groups on the surface of GO were modified completely by organosilicon modifications, for the –OH and –COOH groups diminished the coulomb efficiency. The coulomb efficiencies of GO, 5Si-rGO and 9Si-rGO recovered to the 85.3%, 93.4% and 98.3%, respectively, on the second cycle. In addition, the GO, 5Si-rGO and 9Si-rGO exhibited the similar tendencies that Coulomb efficiencies showed at 100%, after cycling the charge-discharge 100 times (Figure 5(b)).

Moreover, the 9Si-rGO showed cycling performance at 901 mA h g^{-1} after cycling 200 times, which was higher than the GO showing at 159 mA h g^{-1} and 5Si-rGO showing at 260 mA h g^{-1}, respectively (Figure 5(c)). The 9Si-rGO exhibited the relatively excellent Li$^+$ storage at 446 mA h g^{-1} under 2.0 A/g and maintained the high capacity retention rate at 97%, after cycling the charge-discharge 300 times (Figure 6). The reasons about the decrease of Li$^+$ storage at current density of 2.0 A/g are explained by Zhao et al. [34]. In spite
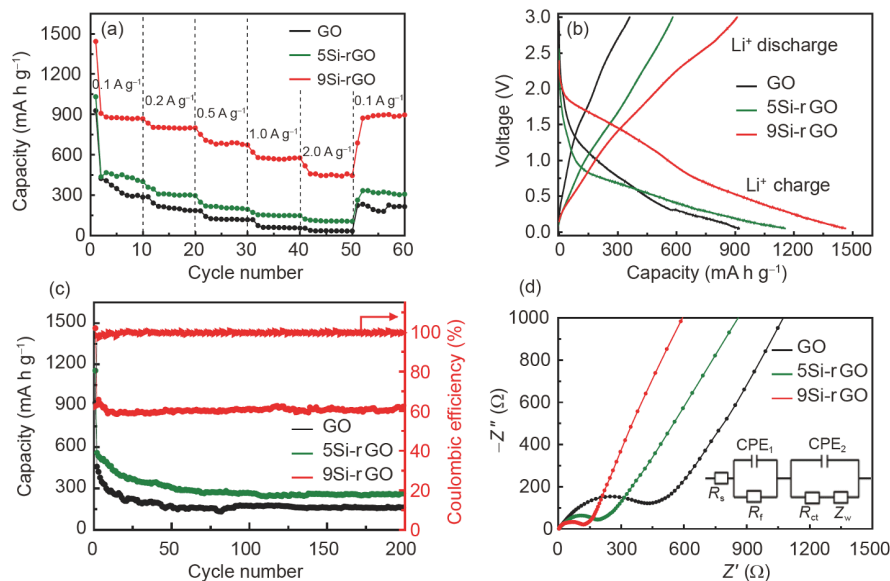
Figure 5 (Color online) Electrochemical performances of GO and organosilicon MrGO. Rate performances (a), charge-discharge capacity (b), cycling performances (c) and nyquist plot results (d). The R_f, R_{ct}, CPE$_1$, CPE$_2$ and Z_W belonging to the equivalent circuit fitting to the plots represent the contact resistance, charge-transfer impedance, constant phase element of the SEI film, constant phase element of the electrode-electrolyte interface and Warburg impedance, respectively.
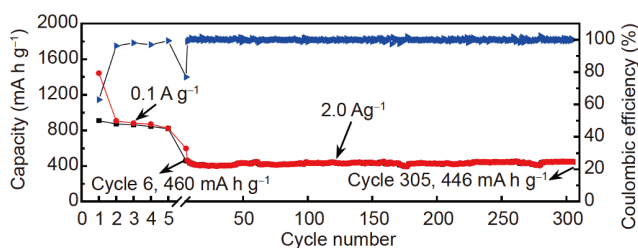

Figure 6 (Color online) Cycling performance of 9Si-rGO electrode at a current of 2.0 A g^{-1} (up to 5 cycles at a current density of 0.1 A g^{-1}).

of fact that storage capacity of 9Si-rGO is not very high, it shows the improved storage capacity, compared with other prepared graphene materials (Table S3).

Figure 5(d) revealed the electrochemical research-impedance results of GO, 5Si-rGO and 9Si-rGO. As a result, the diameter of the semicircle of anode electrodes using 9Si-rGO was much smaller than that of anode electrodes fabricated by GO, and 5Si-rGO, leading us to consider that 9Si-rGO electrode owns lower charge-transfer impedances. On the other hand, based on the reports of Lou et al. [35–36], R_{ct} values were simulated to the 460.2, 185.7 and 91.2 Ω, respectively, referring to the equivalent circuit fitting to the plots (Table S4). These results also reveal the 9Si-rGO owns more excellent conductivity than the GO and 5Si-rGO, respectively. As a consequent, the increased conductivity contributed to the improvement of rate performances of 9Si-rGO.

The kinetic differences between GO, 5Si-rGO and 9Si-rGO were further confirmed by σ value of Warburg coefficient in Figure 7. The σ value could be obtained by measurement of the Randles plot which is plotting of Z' with $\omega^{-1/2}$
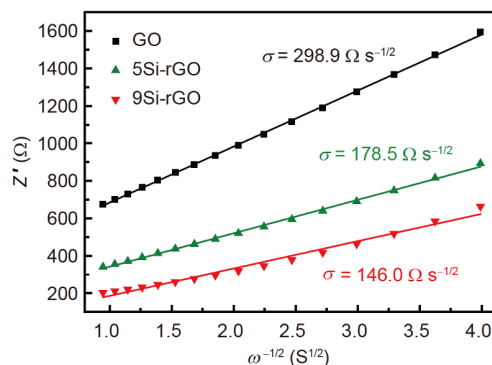

Figure 7 (Color online) Illustrations of relationships between Z' and $\omega^{-1/2}$ in the low-frequency region.

($\omega = 2\pi f$) for a low-frequency [37]. The larger value of σ is able to reflect the poor ion diffusion performance. As a result, the σ corresponding values of GO, 5Si-rGO and 9Si-rGO were calculated as 298.9, 178.5 and 146.0 Ω s$^{-1/2}$, respectively, indicating the 9Si-rGO possessed the remarkably higher Li$^+$ transfer than GO and 5Si-rGO. These above results from impedance measurements are suggestive of that 9Si-rGO owned the extremely more excellent electron/ionic conductivity than the GO and 5Si-rGO, which also causes that 9Si-rGO has more excellent rate performance than GO and 5Si-rGO [38].

Finally, to understand the Li$^+$ storage mechanism, we performed the dynamic analysis by the CV curves at scan rate from 0.2 to 3.0 mV s^{-1}, based on the reports of Wang et al. [39]. According to the dynamic analysis using CV measurement results at sweep rate of 3 mV s^{-1}, the 9Si-rGO
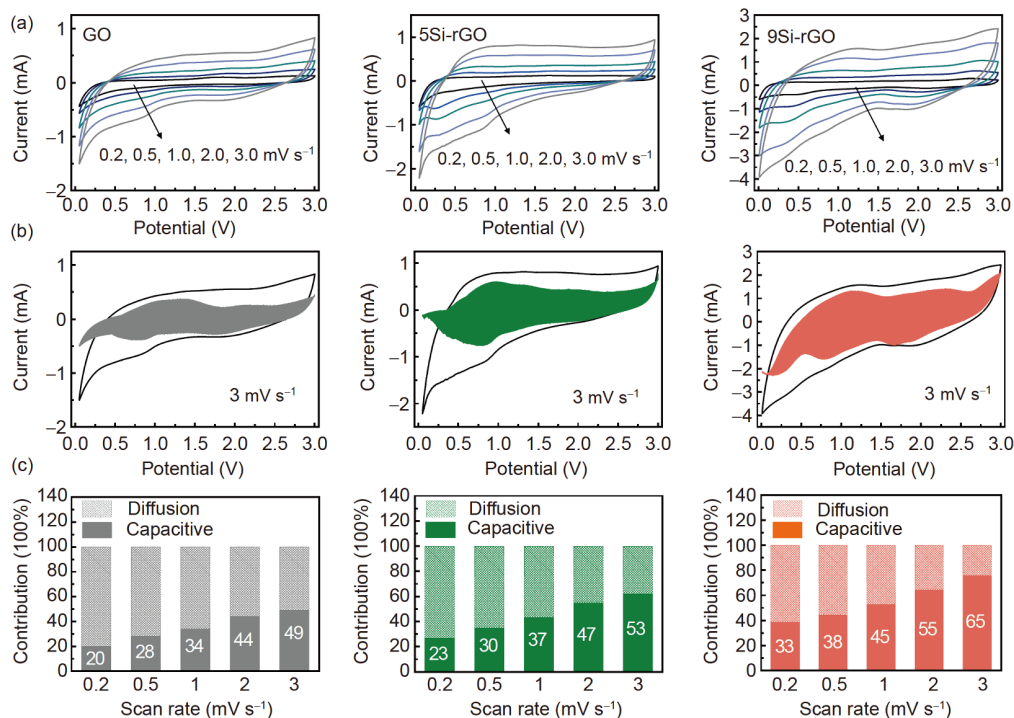
Figure 8   (Color online) The capacitive contributions in storage capacity of GO, 5Si-rGO and 9Si-rGO are illustrated. Thereinto, (a) the CV measurement results at different scan rates; (b) the CV curves with capacitive fraction demonstrated by the shaded area at a scan rate of 3 mV s^{-1}; (c) the bar charts showing the percent of capacitive contribution at different scan rates.

shows the relatively higher capacitive contribution at (65%) than GO (49%) and 5Si-rGO (53%) (Figure 8). Furthermore, the 9Si-rGO shows the relatively higher Li$^+$ storage capacity than the 5Si-rGO and GO at different scan rates (Table S5). It is considerable that introducing of organosilicon groups is able to increase the capacitive effect, for the oxygen element on the –COSiR$_3$ and –COOSiR$_3$ groups can provide the surface reaction sites and defects for Li$^+$ storage [40–41].

4   Conclusion

In summary, the organosilicon groups were successfully introduced on the surface of GO, causing that organosilicon MrGO possesses the 3D rGO-like structure. The Li$^+$ storage capacity of organosilicon MrGO is improved obviously, compared to the GO. The introducing of organosilicon groups increased the capacitive effect, for organosilicon groups on the surface of MrGO can provide the surface reaction sites and defects for Li$^+$ storage. Our studies unveil the organic-inorganic hybrid concept is the effective way to give the improvement of Li$^+$ storage to the general carbon materials such as GO.

Supporting Information

The supporting information is available online at tech.scichina.com and link.springer.com. The supporting materials are published as submitted, without typesetting or editing. The responsibility for scientific accuracy and content remains entirely with the authors.

1   Novoselov K S, Geim A K, Morozov S V, et al. Two-dimensional gas of massless Dirac fermions in graphene. Nature, 2005, 438: 197–200
2   Sun X, Zhou C, Xie M, et al. Amorphous vanadium oxide coating on graphene by atomic layer deposition for stable high energy lithium ion anodes. Chem Commun, 2014, 50: 10703–10706
3   Sun D, Yang J, Yan X. Hierarchically porous and nitrogen, sulfur-codoped graphene-like microspheres as a high capacity anode for lithium ion batteries. Chem Commun, 2015, 51: 2134–2137
4   Yu P C, Yuan Y C. One-step synthesis of robust carbon nanotube foams with ultrahigh surface area for high-performance lithium ion battery. Sci China Tech Sci, 2019, 62: 464–471
5   Wu K, Du K, Hu G. A novel design concept for fabricating 3D graphene with the assistant of anti-solvent precipitated sulphates and its Li-ion storage properties. J Mater Chem A, 2018, 6: 3444–3453
6   Yu J, Huang H, Gan Y, et al. A new strategy for the construction of 3D TiO$_2$ nanowires/reduced graphene oxide for high-performance lithium/sodium batteries. J Mater Chem A, 2018, 6: 24256–24266
7   Wang X, Ai W, Li N, et al. Graphene-bacteria composite for oxygen reduction and lithium ion batteries. J Mater Chem A, 2015, 3: 12873–12879
8   Zhao D, Zhu H, Wu C, et al. Facile synthesis of magnetic Fe$_3$O$_4$/graphene composites for enhanced U(VI) sorption. Appl Surf Sci, 2018, 444: 691–698
9   Wang X, Li S D, Sun Y K, et al. Antimony selenide nanorods decorated on reduced graphene oxide with excellent electrochemical properties for Li-Ion batteries. J Electrochem Soc, 2017, 164: 2922–2929

10   Du Z, Ai W, Sun C, et al. Engineering the Li storage properties of graphene anodes: Defect evolution and pore structure regulation. ACS Appl Mater Interfaces, 2016, 8: 33712–33722

11   Amiinu I S, Zhang J, Kou Z, et al. Self-organized 3D porous graphene dual-doped with biomass-sponsored nitrogen and sulfur for oxygen reduction and evolution. ACS Appl Mater Interfaces, 2016, 8: 29408–29418

12   Lu L, De Hosson J T M, Pei Y. Three-dimensional micron-porous graphene foams for lightweight current collectors of lithium-sulfur batteries. Carbon, 2019, 144: 713–723

13   Hou J, Cao C, Idrees F, et al. Hierarchical porous nitrogen-doped carbon nanosheets derived from silk for ultrahigh-capacity battery anodes and supercapacitors. ACS Nano, 2015, 9: 2556–2564

14   Xu G, Qu D, Yu H, et al. Development of electrochemical performances of carbon black obtained by the surface organosilicon-modified method. Russ J Appl Chem, 2016, 89: 1019–1026

15   Chen W, Chen C, Xiong X, et al. Coordination of surface-induced reaction and intercalation: Toward a high-performance carbon anode for sodium-ion batteries. Adv Sci, 2017, 4: 1600500

16   Chen R, Yu Z J, Liu Y, et al. Effects of binders on the electrochemical performance of SnO_2/graphene anode material. Chem Ind Eng, 2014, 31: 45–49

17   Boehm H P, Diehl E, Heck W, et al. Surface oxides of carbon. Angew Chem Int Ed Engl, 1964, 3: 669–677

18   Xia Y, Fang R, Xiao Z, et al. Supercritical fluid assisted biotemplating synthesis of Si–O–C microspheres from microalgae for advanced Li-ion batteries. RSC Adv, 2016, 6: 69764–69772

19   Contarini S, Howlett S P, Rizzo C, et al. XPS study on the dispersion of carbon additives in silicon carbide powders. Appl Surf Sci, 1991, 51: 177–183

20   Chen K, Song S, Liu F, et al. Structural design of graphene for use in electrochemical energy storage devices. Chem Soc Rev, 2015, 44: 6230–6257

21   Xu Y, Lin Z, Zhong X, et al. Solvated graphene frameworks as high-performance anodes for lithium-ion batteries. Angew Chem Int Ed, 2015, 54: 5345–5350

22   Ge Z, Wu D, He L, et al. Effects of graphene oxides on transport and deposition behaviors of bacteria in saturated porous media. Sci China Tech Sci, 2019, 62: 276–286

23   Liu K, Guo Y L, Liu Y Q. Recent progress in stretchable organic field-effect transistors. Sci China Tech Sci, 2019, 62: 1255–1276

24   Liu X W, Li M, Liu F Y, et al. Cotransport of graphene oxides/reduced graphene oxides with BPA in both bare and iron oxides coated quartz sand. Sci China Tech Sci, 2019, 62: 1896–1906

25   Tang J, Chen G, Yang J, et al. Silica-assistant synthesis of three-dimensional graphene architecture and its application as anode material for lithium ion batteries. Nano Energy, 2014, 8: 62–70

26   Liu F, Song S, Xue D, et al. Folded structured graphene paper for high performance electrode materials. Adv Mater, 2012, 24: 1089–1094

27   Ullah N, Shah S A, Xie M, et al. 3D graphene decorated with hexagonal micro-coin of $Co(OH)_2$: A competent electrocatalyst for hydrogen and oxygen evolution reaction. Int J Hydrogen Energy, 2019, 44: 14770–14779

28   López V, Sundaram R S, Gómez-Navarro C, et al. Chemical vapor deposition repair of graphene oxide: A route to highly-conductive graphene monolayers. Adv Mater, 2009, 21: 4683–4686

29   Liu Z, Xiao K, Guo H, et al. Nitrogen-doped worm-like graphitized hierarchical porous carbon designed for enhancing area-normalized capacitance of electrical double layer supercapacitors. Carbon, 2017, 117: 163–173

30   Herrmann I, Kramm U I, Radnik J, et al. Influence of sulfur on the pyrolysis of CoTMPP as electrocatalyst for the oxygen reduction reaction. J Electrochem Soc, 2009, 156: 1283–1292

31   Shi M M, Bao D, Li S J, et al. Anchoring PdCu amorphous nanocluster on graphene for electrochemical reduction of N_2 to NH_3 under ambient conditions in aqueous solution. Adv Energy Mater, 2018, 8: 1800124

32   Ferrari A C, Robertson J. Interpretation of Raman spectra of disordered and amorphous carbon. Phys Rev B, 2000, 61: 14095–14107

33   Zhang J P, Yang Y F, Li B C, et al. A method of fabrication of lithium-ion battery separators with super hydrophobicity and excellent electrolyte infiltration. CN Patent, 201910081393.6, 2019-05-17

34   Zhao N, Wu S, He C, et al. One-pot synthesis of uniform Fe_3O_4 nanocrystals encapsulated in interconnected carbon nanospheres for superior lithium storage capability. Carbon, 2013, 57: 130–138

35   Lou X, Lin C, Luo Q, et al. Crystal structure modification enhanced $FeNb_{11}O_{29}$ anodes for lithium-ion batteries. ChemElectroChem, 2017, 4: 3171–3180

36   Cheng Q, Liang J, Lin N, et al. Porous $TiNb_2O_7$ nanospheres as ultra long-life and high-power anodes for lithium-ion batteries. Electrochim Acta, 2015, 176: 456–462

37   Liu B, Zhao X, Xiao Y, et al. High-surface-area F-doped amorphous MoO_x with high-performance lithium storage properties. J Mater Chem A, 2014, 2: 3338–3343

38   Liu F, Xue D F. Electrochemical energy storage applications of "pristine" graphene produced by non-oxidative routes. Sci China Tech Sci, 2015, 58: 1841–1850

39   Wang J, Polleux J, Lim J, et al. Pseudocapacitive contributions to electrochemical energy storage in TiO_2 (anatase) nanoparticles. J Phys Chem C, 2007, 111: 14925–14931

40   Chen K, Song S, Xue D. Beyond graphene: Materials chemistry toward high performance inorganic functional materials. J Mater Chem A, 2015, 3: 2441–2453

41   Deng Q, Fan C, Wang L, et al. Organic potassium terephthalate $(K_2C_8H_4O_4)$ with stable lattice structure exhibits excellent cyclic and rate capability in Li-ion batteries. Electrochim Acta, 2016, 222: 1086–1093